Discrete Dipole Approximation for Low-Energy Photoelectron Emission from NaCl Nanoparticles

Matthew J. Berg,[1] Kevin R. Wilson,[2] Chris Sorensen,[3] Amit Chakrabarti,[3] and Musahid Ahmed[2]

[1]*Department of Physics & Astronomy, Mississippi State University, Mississippi State, MS 39762*
[2]*Chemical Sciences Division, Lawrence Berkeley National Laboratory, Berkeley, CA 94720*
[3]*Department of Physics, Kansas State University, Manhattan, KS 66506*

Abstract

This work presents a model for the photoemission of electrons from sodium chloride nanoparticles 50-500 nm in size, illuminated by vacuum ultraviolet light with energy ranging from 9.4-10.9 eV. The discrete dipole approximation is used to calculate the electromagnetic field inside the particles, from which the two-dimensional angular distribution of emitted electrons is simulated. The emission is found to favor the particle's geometrically illuminated side, and this asymmetry is compared to previous measurements performed at the Lawrence Berkeley National Laboratory. By modeling the nanoparticles as spheres, the Berkeley group is able to semi-quantitatively account for the observed asymmetry. Here however, the particles are modeled as cubes, which is closer to their actual shape, and the interaction of an emitted electron with the particle surface is also considered. The end result shows that the emission asymmetry for these low-energy electrons is more sensitive to the particle-surface interaction than to the specific particle shape, i.e., a sphere or cube.

1.0 Introduction

The interaction of ionizing radiation with nanoparticles is important to understanding a variety of phenomena ranging from atmospheric nucleation to the heating of dust clouds by secondary electron emission from interstellar grains [wilson_review, draine]. Photoelectron emission (PE) is currently being used as an analytical probe of soot formation within flames, the detection of diesel emission, as spectroscopic probes of micron-sized droplet surfaces, sub-nanometer particles, and bio-aerosols [mitchell, burtscher, starr, grimm, wilson_peterka]. A number of fundamental studies of nanoparticles, 5-200 nm in size, have revealed both unexpectedly large PE quantum yields and circular dichroism, the magnitude of which depends upon particle size [schmidt-ott, kasper]. In many of these studies, the role that particle size and shape play in both the electromagnetic absorption and PE remains an active area research.

In a recent publication, Wilson *et al.* measure the two-dimensional angular distributions of photoelectrons emitted from sodium chloride (NaCl) nanoparticles exposed to vacuum ultraviolet (VUV) light at various photon energies around 10 eV. The key finding is the observation of an asymmetry in the angular PE distribution. At photon energies where the electromagnetic absorption length in the NaCl material is on the order of, or less than, the nanoparticle size

emission is observed preferentially from the geometrically illuminated side of the particles relative to their shaded side. Moreover, this asymmetry is inversely proportional to the particle size.

To investigate the cause and possible utility of this asymmetry, Wilson *et al.* employ a model the emission process in which the particles are approximated as spheres and the PE trajectory within the particle is treated ballistically. Approximating the particles as spheres allows Mie theory to be used to calculate the internal (VUV) electromagnetic field from which emission is initiated. This model is able to reproduce the general trend of the observed PE asymmetry, leading to the conclusion that the asymmetry is due to the nonuniform illumination of the particle interior caused by electromagnetic absorption. However, the agreement between the measured and modeled asymmetry is loose enough to suggest that a more sophisticated treatment could better fit the measurements and hence improve understanding of its cause. The following will describe such a model and compare its results to that reported in the Wilson *et al*.

2.0 Model description

In the measurements, VUV light generated by the Advanced Light Source (ALS) synchrotron at the Lawrence Berkeley National Laboratory is used to illuminate a stream of size-selected NaCl nanoparticles [wilson]. The range of photon energies include 9.4, 10.0, and 10.9 eV, which exceeds the NaCl ionization threshold of 8.2 ± 0.1 eV, and the nanoparticle sizes range from approximately 50-500 nm [taylor, wilson_review]. To acquire two-dimensional angular PE images, electrostatic lenses focus photoelectrons onto a dual multichannel-plate coupled to a phosphor screen, imaged onto a charged coupled device (CCD) camera. The resulting digital image is then numerically analyzed to infer the emission asymmetry.

Figure 1: SEM images (a) of the NaCl nanoparticles used by Wilson *et al.*, and a diagram (b) of the modeled emission process.

The new model developed here begins with a representation of the nanoparticle shape. Figure 1(a) shows scanning electron microscope (SEM) images of the types of nanoparticles used in the measurement. These particles are cube-like in shape with rounded edges and some sign of either surface roughness and/or internal inhomogeneity. As an approximation, a homogeneous cube of length L is taken to represent a particle, see Fig. 1(b). However, spherical model-particles are

also used to understand the effect of particle morphology on the PE emission. In the measurements, each particle enters the VUV beam in a random orientation, which is described in the model using two coordinate systems called the laboratory and particle-systems, (x_L, y_L, z_L) and (x_P, y_P, z_P), respectively. These systems share a common origin at the particle center, and the *z*-axis of the laboratory system is taken along the propagation direction of the VUV beam.

The electric field of the VUV light, which will be called the incident field $\mathbf{E}^{inc}$, is taken to be a linearly polarized plane wave

$$\mathbf{E}^{inc}(\mathbf{r}) = E_o \exp(ik\hat{\mathbf{n}}^{inc} \cdot \mathbf{r}), \tag{1}$$

where $\hat{\mathbf{n}}^{inc}$ describes the propagation direction, and E_o is a constant proportional to the light intensity. Meanwhile, the x_L and y_L-axes are taken along the particle-beam direction, and the direction from the origin to the detector, respectively, refer to Fig. 1(b).

The relative orientation of the two coordinate systems is described by the Euler rotation angles (α, β, γ); transformation between the systems is accomplished by the rotation matrices $\ddot{\boldsymbol{\beta}}$ and $\ddot{\boldsymbol{\beta}}^{-1}$ [MLT]. A random particle-orientation can be realized by choosing three random numbers $\{x_1, x_2, x_3\}$ in the interval [0,1] from which the Euler angles are calculated as

$$\alpha = 2\pi x_1, \quad \beta = \cos^{-1}(2x_2 - 1), \; \gamma = 2\pi x_3. \tag{2}$$

Defining N_{ori} sets of Euler angles this way results in a collection of as many particle orientations sampled randomly from all directions [morawiec].

Next, the electric field $\mathbf{E}^{int}$ inside of the particle is found for each orientation. This is done using the Discrete Dipole Approximation (DDA), which in essence is a numerically exact way to solve the Maxwell equations for any particle, see [yurkin]. To implement the DDA however, requires knowledge of the nanoparticle refractive index m, which is estimated to be $m = 1.79 + 0.55i$ for a photon energy of 9.4 eV, $m = 1.7 + 0.64i$ for 10.0 eV, and $m = 2.15 + 0.60i$ for 10.9 eV [miyata]. The "approximation" in the DDA is that the particle is represented by a collection of coupled electric-dipoles that reside on a cubic lattice spanning the particle volume. Thus, the accuracy of the calculation is determined by the fineness of this lattice. Typically, one uses a lattice spacing that is roughly $\lambda'/10$, where λ' is the (refracted) wavelength in the particle material [yurkin]. Given the photon energies considered and associated refractive indexes, the smallest refracted wavelength is $\lambda' = 52.9$ nm, and hence a lattice spacing corresponding to $l = 5$ nm is used.

Other techniques to find the electromagnetic field in nonspherical particles are available, however, the DDA is well-suited for this application because the shape of the model particle exactly coincides with the dipole lattice geometry. Consequently, the sharp corners and edges of the particle, which typically cause enhancements in the field magnitude, are not problematic in these DDA calculations. Figure 2 shows an example of the surface field magnitude for two cubic particles, one with and one without absorption. The absorbent particle corresponds to a size and refractive index consistent with those in the measurements.

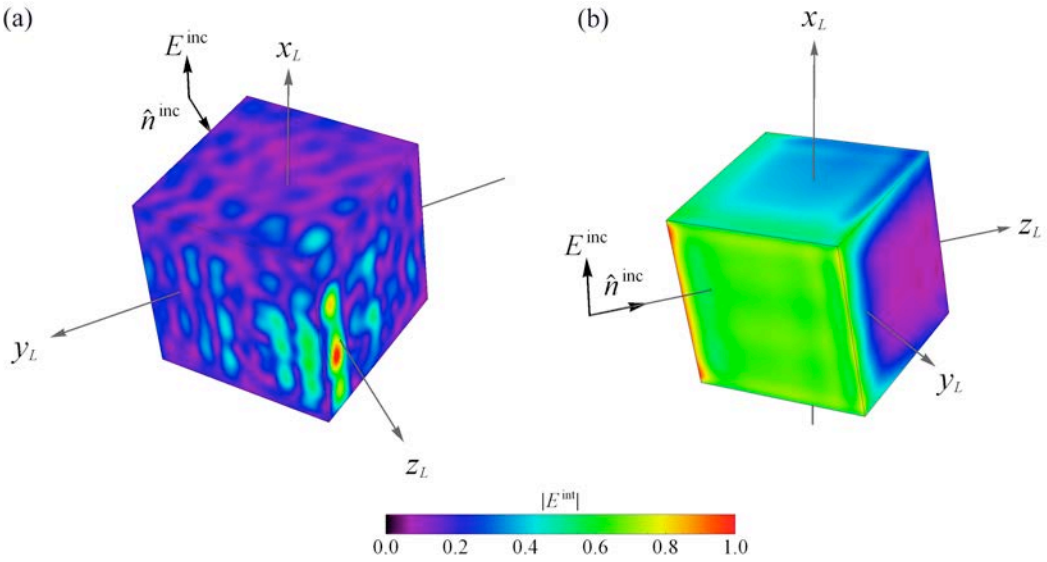

Figure 2: Examples of the electric field magnitude at the surface of a cubic nanoparticle calculated using the DDA. The particle in (a) has refractive index $m = 1.79 + 0i$ and hence is nonabsorbent, unlike the particles in the measurements and the one shown in (b) where $m = 1.79 + 0.55i$. Comparison between the two shows that a strong enhancement in the field occurs on the side of the nonabsorbent particle where the incident light leaves it, i.e., along the positive z_L-axis. This is an example of a so-called hot spot, which does not occur for the absorbent particle. Rather, the large field magnitude for absorbing particle occurs along the edges and corners of the geometrically illuminated side, which can be seen in (b). Note that the perspective of the two particle is different; particle back-side view in (a) and particle-side view in (b).

Once $\mathbf{E}^{int}$ is known at each lattice site $\mathbf{r}_s$ in the particle, the PE can be simulated. This process is in-part based on Wilson *et al.* and includes the following steps that are performed at each site for each particle orientation:

(1) A random direction $\hat{\mathbf{r}}_e$ for electron emission is chosen following Eq. (2) and is represented by the corresponding Euler angles $\{\alpha_e, \beta_e, \gamma_e\}$.

(2) The straight-line distance d from $\mathbf{r}_s$ to the particle surface along the direction $\hat{\mathbf{r}}_e$ is found.

(3) An emission probability P is then assigned to this electron according to

$$P = c\,|\,\mathbf{E}^{int}\,|^2\,\sin\theta\,\sin^2\delta\,e^{-d/r_{mfp}} \qquad (3)$$

where θ is the polar angle in the laboratory frame, i.e., the angle between $\hat{\mathbf{r}}_e$ and $\hat{\mathbf{n}}^{inc}$, δ is the angle between $\hat{\mathbf{r}}_e$ and $\mathbf{E}^{int}$ at the site, r_{mfp} is the electron mean free path, and c is a normalization factor.

(4) The angle between the particle-surface normal $\hat{\mathbf{n}}$ and $\hat{\mathbf{r}}_e$ at the point where the (linear) electron trajectory intersects the particle-surface is found. This angle, denoted ξ is compared to the so-called escape-cone angle θ_{esc}; if $\xi \le \theta_{esc}$ then the electron is counted as leaving the particle, but is not if $\xi > \theta_{esc}$.

Figure 2 shows a sketch illustrating the angles and vectors involved in this emission process. The factor of $\sin\theta$ in Eq. (3) accounts for the weighting associated with integration over the polar

angle, while the factor $\sin^2\delta$ accounts for the angular dependence of PE from a lattice site assuming dipole excitation [wilson]. The inclusion of the escape-cone angle was not implemented in the Wilson *et al*. model. Use of this angle to restrict which electron trajectories contribute to particle ionization has been proposed before, but has not been implemented in a sophisticated model like is done here, see [ferrini]. In short, this angle requires that an electron overcome a surface potential before it is permitted to completely leave the particle. One will see below that this angle significantly affects the emission asymmetry α.

Figure 3: Diagram showing a particle along with the vectors and angles used to model the emission process. Also indicated is the propagation direction of the VUV light $\hat{\mathbf{n}}^{\text{inc}}$, and the forward and backward hemispheres used to calculate the PE asymmetry parameter α described below.

Once an electron has left the particle, it is accelerated to the detector plane by an external static field $\mathbf{E}^{\text{ext}}$, and examples of the resulting parabolic electron trajectories are shown in Fig. 1(b). To simulate the measured detector-images, this plane is divided into an array of 64 x 64 pixels. The probability P given to each electron in step (2) is then assigned to the pixel within which it intercepts the plane. If more than one electron intercepts a given pixel, the associated probabilities are added, then the entire array is normalized by the largest pixel value after all particle orientations have been considered. The resulting distribution tends to be disk-like in shape, as seen below in Fig. 4, due to the multiple particle-orientations used.

3.0 Emission asymmetry

Figure 4 shows a comparison of the measured (left) and modeled (right) two-dimensional angular PE images at various photon energies and for various particle sizes. In the measurements, the size is described in terms of the radius R of a sphere that just fits inside a cube of length L, i.e., $R = L/2$. For the model, the electron mean free path and escape-cone angle are $r_{\text{mfp}} = 10.0$ nm and $\theta_{\text{esc}} = \pi/4$, respectively. Note that as discussed at the end of this section, this choice for r_{mfp} and θ_{esc} gives results that best fit the measurements when a cube is used as the model particle. However, the value for θ_{esc} giving acceptable agreement with measurement is different

if a spherical model-particles are used. One can see that the emission displays a pronounced asymmetry. More photoelectrons are emitted into the forward hemisphere, which consists of directions with negative projection along the z_L-axis, as compared to the backward hemisphere, i.e., emission directions with positive z_L-axis projections. The projection of these hemispheres onto the detector plane corresponds to the top and bottom half of the images, respectively. Qualitatively, the measured and modeled images agree reasonably well. One can see that as the particle size increases for a given photon energy, more emission into the forward hemisphere is seen, revealing that the emission originates more from the geometrically illuminated side of a particle. The measurement images show regions of peak emission, i.e., yellow, over a larger extent of the image than do the model images. In the modeled images the peak emission localized more to the top of the image. A possible explanation for this apparent discrepancy is that measured images shown are not corrected for variations in the particle positions within the VUV beam, whereas the particles in the model are always at the origin when emission is simulated. The consequence of varying particle-position in the measurement consisting of an ensemble of many individually illuminated particles can be to smear the angular structure of the net emission. Such a distortion of the PE distribution could account for the qualitative difference seen in Fig. 4.

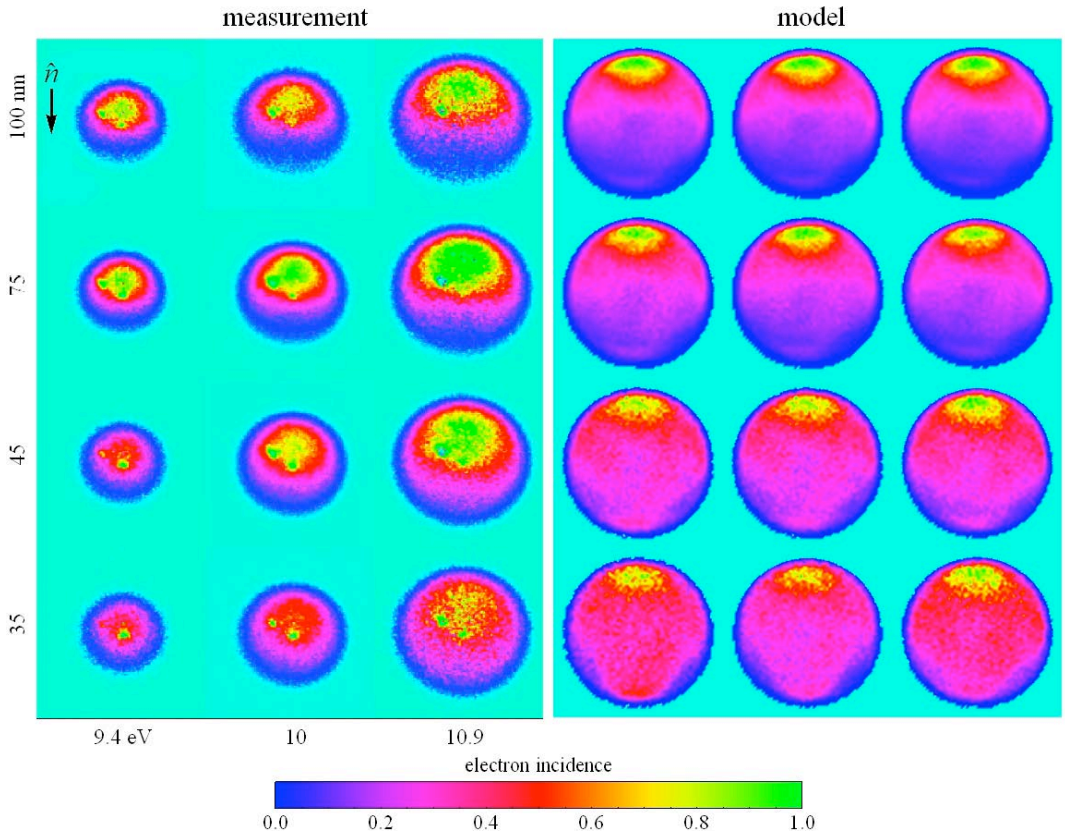

Figure 4: Measured and modeled two-dimensional angular PE images. The propagation direction of the VUV light is indicated by the arrow in the top left, recall Fig. 1(b). The particle equivalent-sphere radii and photon energy labeled on the measured images also apply to the modeled ones.

To better quantify the emission asymmetry, the top and bottom halves of the detector images are integrated, and the ratio of the resulting values defines the asymmetry parameter α. If $\alpha = 1$, photoelectrons are emitted equally into the forward and backward hemispheres, whereas if $\alpha < 1$ more electrons are emitted into the forward hemisphere relative to the backward hemisphere,

recall Fig. 3. Figure 5 presents a series of comparisons between the measured α as a function of equivalent-sphere particle size R for photon energies of 9.8 and 10.9 eV, and the modeled α using either spheres or cubes. The rational for considering a sphere as a model particle here is to connect with the work done in Wilson *et al*. This provides a degree of validation for the DDA-based model in addition for giving a sense of the affect that the model-particle shape has on α.

The curves presented in Fig. 5(a) are generated using a sphere as the model particle, but otherwise following exactly the same procedure as described in Sec. 2. Here, the photon energy is 10.9 eV and the escape-cone angle is varied from $\pi/2$ to $3\pi/8$ to show how this parameter affects the asymmetry. Note that the curve for $\theta_{esc} = \pi/2$ would correspond to the model curve presented in Wilson *et al.* The best agreement with the measurements is seen when $\theta_{esc} = 3\pi/8$ and the electron mean free path is $r_{mfp} = 10.0\,\text{nm}$, the latter of which is consistent with Wilson *et al*. and expectations from the literature.

Figure 5: Measured and modeled asymmetry-parameter curves as a function of particle radius using spheres and cubes as the model-particle shape. The measured data is shown for 9.8 and 10 eV only, whereas the modeled curves are presented for the same energies as in Fig. 4.

Figure 5(b)-(d) uses cubes as the model particles. In these plots, both r_{mfp} and θ_{esc} are varied using three photon energies to investigate whether the more-realistic particle shape improves the agreement between the modeled and measured asymmetry. As with the spherical model-particle, the overall effect of decreasing the escape cone angle is to reduce the asymmetry. Moreover, this effect appears to be largely independent of the photon energy and mean free path, cf. plots (c) and (d). Asymmetry curves generated using $r_{mfp} = 10.0$ nm and $\theta_{esc} = \pi/2$ appear nearly identical

to those shown in Fig. 5(b) where $r_{\mathrm{mfp}} = 4.72$ nm, and hence are not shown here. This demonstrates however, that variation in the mean free path is less influential on the asymmetry than the escape-cone angle. The best agreement to the measurements occurs when $\theta_{\mathrm{esc}} = \pi/4$ and $r_{\mathrm{mfp}} = 10.0$ nm [plot (c)], although surprisingly, the agreement is not as good as that seen when a sphere is used as the model particle, i.e. plot (a). This result suggests that for these photon energies, the particle shape has less influence on the emission asymmetry than the electron mean free path and escape-cone angle.

4.0 Discussion

One question raised in Wilson *et al.* is whether the difference between the modeled and measured asymmetry is due to the approximation of the nanoparticle shape as a sphere or is due to the simple ballistic electron-transport used. The results above suggest that approximations of the particle shape and electron transport have weaker consequences on the emission asymmetry than accounting for an electron's interaction with the particle surface. From the point of view of the energies involved, this seems plausible: The energies considered are at most 2.7 eV above the ionization threshold of 8.2 ± 0.1 eV for bulk NaCl [wilson_review]. Then, an electron liberated from a lattice site within the nanoparticle has low kinetic energy compared to this threshold as it emerges from the particle surface. Electrostatic image-forces may then affect the electron's initial trajectory. The escape-cone cutoff angle is, in a sense, a "first-order" way to build in this interaction into the model.

With regard to which model-particle shape is more appropriate, the results show that spheres fit the measurements slightly better than cubes, recall Fig. 5. One may find this surprising given that the crystal structure of NaCl is cubic. However, the SEM images of the particles in Fig. 1 reveal that the edges and corners of the cubic particles are rounded, more resembling a sphere-like shape in some cases. In addition, the measured PE images are the result of contributions from many randomly oriented particles. It is plausible then that much of the nonspherical-shape signatures in the angular emission distribution are washed out by the averaging of these may orientations. In other words, one might expected to see much more structure in the PE image corresponding to a *single* particle measurement than is seen in Fig. 4. Unfortunately, such measurements are not available for comparison, but with the development of ultrafast extreme ultraviolet and X-ray lasers that can probe the electronic dynamics of single nanoparticles using photoemission, new measurements of how particle shape couples with electron escape dynamics might be possible in the future.

Acknowledgments
We thank the Kansas State University electron microscope facility for the SEM images of the NaCl particles used in this work. This work was partly supported by the NASA Graduate Student Researchers Program. K.R.W and M.A. are supported by the Director, Office of Energy Research, Office of Basic Energy Sciences, Chemical Sciences Division of the U.S. Department of Energy under Contract No. DE-AC02-05CH11231.

References

[wilson_review] K. R. Wilson, H. Bluhm, and M. Ahmed, "Aerosol photoemission," in *Fundamentals and Applications in Aerosol Spectroscopy*, R. Signorell and J. P. Reid eds., CRC press (2010).
[draine] B. T. Draine, "Interstellar dust grains," Annual Rev. Astron. Astrophys. **41** p. 241-289 (2003).

[mitchell] J. B. A. Mitchell, C. Rebrion-Rowe, J. L. Legarrec, G. Taupier, N. Huby, "X-ray synchrotron radiation probing of an ethylene diffusion flame," Combust. Flame **131** p. 308-315 (2002).

[Burtscher] H. Burtscher, A. Schmidt-Ott, H. C. Siegmann, "Monitoring Particulate-Emissions from Combustions by Photoemission," Aerosol Sci. Tech. **8** p. 125-132 (1988).

[starr] D. E. Starr, E. K. Wong, D. R. Worsnop, K. R. Wilson, H. Bluhm, "A combined droplet train and ambient pressure photoemission spectrometer for the investigation of liquid/vapor interfaces," Phys. Chem. Chem. Phys. **10** p. 3093-3098 (2008).

[grimm] M. Grimm, B. Langer, S. Schlemmer, T. Lischke, U. Becker, W. Widdra, D. Gerlich, R. Flesch, E. Rühl, "Charging mechanisms of trapped element-selectively excited nanoparticles exposed to soft X rays." Phys. Rev. Lett. **96** p. 1-4 (2006).

[wilson_peterka] K. R. Wilson, D. S. Peterka, M. imenez-Cruz, S. R. Leone, M. Ahmed, "VUV photoelectron imaging of biological nanoparticles: Ionization energy determination of nanophase glycine and phenylalanine-glycine-glycine," Phys. Chem. Chem. Phys. **8** p. 1884-1890 (2006).

[schidt-ott] A. Schmidt-Ott, P. Schurtenberger, H. C. Siegmann, "Enormous yield of photoelectrons from small particles," Phys. Rev. Lett. **45**, p. 1284-1287 (1980).

[kasper] M. Kasper, A. Keller, J. Paul, K. Siegmann, H. C. Siegmann, "Photoelectron spectroscopy without vacuum: nanoparticles in gas suspension," J. Electron Spectrosc. Relat. Phenom. **98-99** p. 83-93 (1999).

[wilson] K. R. Wilson, S. Zou, J. Shu, E. Ruhl, S. R. Leone, G. C. Schatz, and M. Ahmed, "Size-dependent angular distributions of low-energy photoelectrons emitted from NaCl nanoparticles," Nano Lett., **7** p. 2014-2019 (2007).

[taylor] J. W. Taylor, and P. L. Hartman, "Photoelectric effects in certain of the alkali halides in the vacuum ultraviolet," Phys. Rev. **113**(6) p. 1421-1435 (1959).

[MLT] M. I. Mishchenko, L. D. Travis, and A. A. Lacis, *Scattering, Absorption, and Emission of light by Small Particles*, Cambridge (2002).

[morawiec] A. Morawiec, *Orientations and Rotations*, Berlin: Springer (2004).

[yurkin] M. A. Yurkin and A. G. Hoekstra, "The discrete dipole approximation: an overview and recent developments," J. Quant. Spectrosc. Radiat. Transfer **106** p. 558-589 (2007).

[miyata] T. Miyata, T. Tomiki, "Optical studies of NaCl single crystals in 10 eV region II. The spectra of conductivity at low temperatures, absorption constant and energy loss," J. Phys. Soc. Japan **24**(6), p. 1286-1302 (1968).

[ferrini] G. Ferrini, P. Michelato, and F. Parmigiani, "A monte carlo simulation of low energy photoelectron scattering in Cs2Te," Solid State Commun. **106**(1), p. 21-26 (1998).

[akkerman] A. Akkerman, T. Boutboul, A. Breskin, R. Chechik, A. Gibrekhterman, "Low-energy electron transport in alkali halides," J. Appl. Phys. **76** p. 46564662 (1994).